Editors' Suggestion

Coherent turbulence and entrainment in a supersonic, axisymmetric, separated/reattaching shear layer

Branden M. Kirchner,* Gregory S. Elliott,† and J. Craig Dutton‡
University of Illinois at Urbana-Champaign, Department of Aerospace Engineering, Urbana, Illinois, USA

(Received 5 May 2020; accepted 13 July 2020; published 10 August 2020)

The influence of coherent turbulent structures on the entrainment characteristics of a separated shear layer in a Mach-2.49 longitudinal cylinder wake is investigated using stereoscopic particle image velocimetry (SPIV). Three thousand non-time-correlated velocity field measurements, acquired along a plane coincident with the central axis, were decomposed into modes using the snapshot proper orthogonal decomposition (POD) method. The second and third POD modes identified high-energy velocity fluctuations aligned with consistent directions in the separated shear layers, near the boundaries of the recirculation region. Previous work by the authors has demonstrated, using tomographic PIV, that these directionally consistent velocity fluctuations identified by the POD modes are caused by three-dimensional (3D) coherent upright and inverted hairpin vortex structures in this flow. The SPIV velocity field snapshots were conditionally sorted based on the value of their corresponding POD amplitude coefficients, and conditional statistics from these subsets of snapshots were used to derive results in the current work. It is demonstrated that a higher statistical prevalence of upright hairpin vortices in the shear layer directly correlates with reduced shear layer growth rates, and a subsequent increase in the reattachment length. Conversely, a higher statistical prevalence of inverted hairpin vortices correlates with increased shear layer growth rates, and a subsequent reduction in the reattachment length. Comparisons of conditional statistics for the SPIV data are drawn with previous laser Doppler velocimetry measurements acquired in a 5° boat-tailed cylinder configuration of this flow. These comparisons demonstrate clear similarities of important features between the two flows, such as an increase in the reattachment length when compared to the unconditional blunt-based cylinder flow, which is indicative of higher cylinder base pressures and subsequently reduced pressure drag.

DOI: 10.1103/PhysRevFluids.5.084605

I. INTRODUCTION

The turbulence mechanisms of high-speed separated flows are of fundamental importance in many practical applications. Pressure loading in massively separated regions of bluff body wakes can significantly hinder vehicle aerodynamic performance through high-pressure drag, unsteady loading affecting vehicle controllability, and loss of lift. For a separated shear layer reattaching on a wall surface (such as a backward-facing step flow), the local thermal loading near the reattachment point can be high and dictate material requirements. Additionally, for high-speed combustors, the mixing characteristics of the separated shear layer drive the combustion efficiency and overall performance of the engine. Arguably the most dominant feature in all of these flows is the separated

*kirchnr2@gmail.com
†elliottg@illinois.edu
‡jcdutton@illinois.edu

 ©2020 American Physical Society

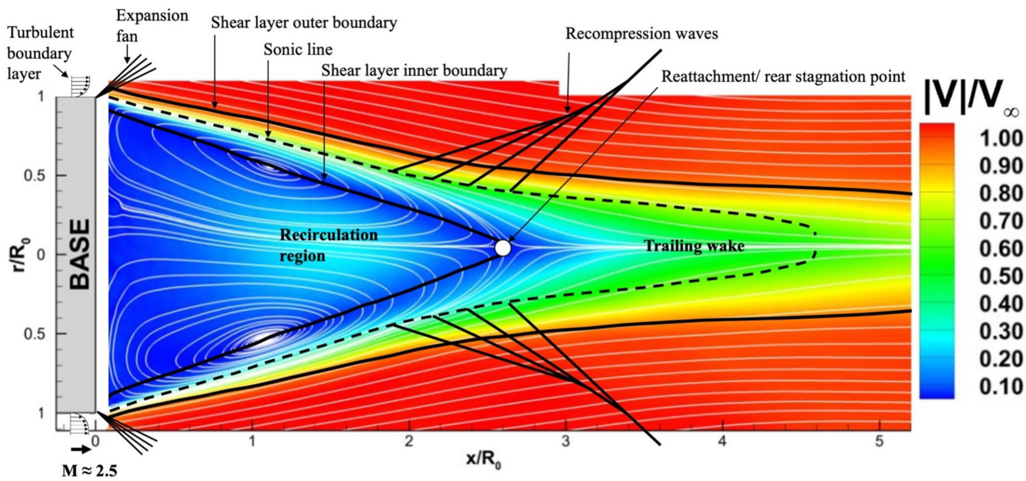

FIG. 1. Data-derived schematic of the time-averaged near-wake flow field.

shear layer, whose growth and entrainment characteristics ultimately drive reattachment length, pressure loading in the separated region, and mixing efficiencies. This creates an obvious motivation to study these separated shear layers, as obtaining a more detailed understanding of the turbulence mechanisms within them could lead to more efficient engineering designs, which better mitigate or control these phenomena.

The particular flow of interest in the current work is the near-wake, massively separated region downstream of a blunt-based cylinder aligned with a Mach-2.49 free stream. This geometry is typically referred to as a "base flow," and is the axisymmetric extension of the more canonical 2D planar base flow [1–3]. An experimental data-derived schematic of the time-averaged flow features of the current flow is shown in Fig. 1, utilizing data that was originally presented in Ref. [4], and will also be utilized throughout the current study.

In the current flow, a fully developed turbulent boundary layer separates from the cylinder body upon reaching the corner of the base. The strong expansion at the base corner turns the flow radially inward, forming the initial condition for a spatially developing, conical, separated shear layer, which is bounded above by the nonturbulent supersonic free stream that has been accelerated by the expansion and below by the turbulent subsonic recirculation region. This conical shear layer eventually converges and reattaches at the rear stagnation point along the central cylinder axis. Information about this reattachment process propagates upstream along the subsonic portions of the shear layer, which induces an elongated region of gradual flow field recompression (i.e., an adverse pressure gradient), wherein the flow realigns itself with the central axis. This recompression region begins some distance upstream of reattachment and extends beyond reattachment into the trailing wake. In the supersonic portions of the flow, this recompression manifests itself in the form of weak shocklets, which eventually coalesce into a finite oblique shock far out in the free stream. Downstream of reattachment, the flow transitions into the trailing wake, which rapidly recovers the central velocity deficit to become fully supersonic. Throughout this work, the trailing wake will refer to any region of the flow downstream of the reattachment point.

Although the geometry of this flow is simple, the resulting flow field is highly turbulent and convoluted, and is dominated by three-dimensional structures [5,6]. For incompressible or weakly compressible shear layers, the dominant instability mechanisms are largely two-dimensional, originating from the Kelvin-Helmholtz instability [7]. At higher compressibility levels, however, such as in the present flow, the dominant instabilities become increasingly oblique, and more three dimensional in nature [8,9]. This is well demonstrated with plan-view qualitative visualizations of turbulent structures in compressible mixing layers by Clemens and Mungal [10], wherein with increased compressibility levels, the structures continually exhibit a decrease in spanwise coherence, ultimately displaying highly three-dimensional geometries. Additionally, the performance capabilities of vehicles that produce this type of base flow wake, such as missiles or ballistic projectiles, are greatly affected by the dynamic pressure loading on the cylinder base that these turbulent structures ultimately induce. In-flight pressure measurements of artillery-fired projectiles demonstrated that the time-averaged pressure drag induced by these flows constitutes approximately 40% of the total vehicle drag, with this contribution toward total drag increasing at higher free-stream Mach numbers [11]. This pressure drag is ultimately the result of the turbulent transfer of fluid mass (i.e., entrainment) between the separated shear layer and the recirculation region.

In this flow field, defining the high-speed boundary of the shear layer is obvious, as the mean shearing vanishes while traversing into the nonturbulent free stream. The low-speed boundary, however, is less obvious, as the mean shearing only vanishes along the central axis from the flow symmetry constraint, which is in the center of the recirculation region. Therefore, in order to treat the shear layer and recirculation region as distinctly separate flow regions, which turbulently interact with one another, a boundary between the two must be defined. One logical approach is to define this boundary as the contour defined by zero axial velocity, which separates recirculated fluid on one side from nonrecirculated fluid on the other. Although this is not a rigorous definition of a shear layer boundary, the contour defining this boundary is commonly used to establish the reattachment length in separated/reattaching shear layers [12] (i.e., the axial velocity vanishes at the reattachment location). Thus, convolutions of this boundary and turbulent interactions across it are surely of importance in the determination of shear layer growth and reattachment length. Additionally, this definition does meet the criteria for a valid turbulent surface given by Pope [13], so its behavior is expected to exhibit characteristics similar to that of more rigorously defined boundaries, such as the commonly used turbulent/nonturbulent interface [14,15]. This definition of the low-speed shear layer boundary is demonstrated in Fig. 1 and is utilized in subsequent figures throughout this paper.

As the recirculation region is fully bounded by the conical shear layer and cylinder base, continuity requirements dictate that the shear layer cannot endlessly entrain fluid from the recirculation region, as it nominally can from the free stream. There must be a time-averaged balance of mass transfers both out of and into the recirculation region (i.e., entrainment and detrainment), respectively. However, the local entrainment/detrainment rates (i.e., the time-averaged quantity of fluid mass flux per unit area) can be modulated and are ultimately determined by the instantaneous turbulent structures within the shear layer. Modifying these entrainment/detrainment rates would directly modify the shear layer growth characteristics and subsequently change the reattachment length. This is because a faster spatially growing shear layer will reattach further upstream, and vice versa for a slower growing shear layer. Additionally, the reattachment length has been demonstrated in the literature to directly correlate with the time-averaged pressure loading in these massively separated/reattaching flows [16]. Therefore, identification and further understanding of the turbulent structures that dominate the instantaneous mass transfers between the recirculation region and separated shear layer will provide essential knowledge in the future development of aerodynamically efficient vehicle designs or flow control methodologies aimed at modulating base pressure loading.

Many studies, both experimental and computational, have been performed over the past several decades to better understand the turbulence mechanisms within this flow. The important works of Herrin and Dutton [12,16–18] in the 1990s, utilizing laser Doppler velocimetry (LDV) measurements, provided significant insights into the statistical distribution of turbulent properties throughout the near-wake flow field. They acquired measurements in the separated region of both the current flow, as well as a 5° boat-tail cylinder configuration. The addition of the boat tail prior to separation demonstrated a modulation of the turbulence structure within the shear layer between the two cases, resulting in a 21% reduction in cylinder pressure drag for the boat-tail case and a corresponding change in reattachment length (i.e., reattachment shifted downstream for the boat-tail cylinder due to reduced mean entrainment/detrainment rates). However, the measurements of turbulence quantities in these studies were acquired on a point-by-point basis, with only two components of velocity, and at relatively low spatial resolution compared to modern experimental standards. These experimental reference LDV data for this flow were recently superseded by the current authors using high spatial resolution stereoscopic particle image velocimetry (SPIV) measurements [4], which increased the spatial density of velocity data over the LDV measurements by a factor of 28, as well as providing all three components of velocity. Additionally, these SPIV measurements acquired simultaneous velocity measurements throughout the entire flow field, which allows for the use of modal decomposition analysis techniques. These same SPIV data are utilized throughout the current work, and the time-averaged flow field resolved by these data was depicted in Fig. 1.

As mentioned previously, the objectives of the current work are to obtain a more thorough understanding of the turbulent mechanisms that dominate the entrainment/detrainment interactions between the separated shear layer and recirculation region of this flow. This is accomplished by analyzing the current SPIV data with the snapshot proper orthogonal decomposition method (POD) [19] and conditionally sorting the data based on the POD modes. In general, the literature on separated shear layer entrainment mechanisms is lacking in comparison to that of unseparated free shear layers [10,20,21]. This becomes increasingly true in highly compressible separated flows, where very few published works on the subject of entrainment mechanisms in these flows exist [22,23].

The remainder of this paper is organized as follows. Section II outlines the methodologies of the current work, including the experimental wind tunnel facility, the SPIV measurements, and a stencil outlining the implementation of the POD analysis. Section III discusses the mean growth rate trends and compressibility levels of the separated shear layer. Section IV discusses the results derived from the POD analysis, and conclusions are given in Sec. V.

II. METHODOLOGIES

A. Wind tunnel facility

Experiments for this study were performed in the axisymmetric supersonic base flow wind tunnel, located in the Gas Dynamics Laboratory at the University of Illinois at Urbana-Champaign. This blowdown facility is powered by a 224-kW electric air compressor, which charges an external storage volume of 132 m^3 to a maximum pressure of 1.03 MPa. The compressed air is filtered and dried to a nominal dew point of approximately 223 K. Air enters the stagnation chamber from the top through a 45° angled pipe, which impinges the flow on the rear flange of the chamber to promote flow stagnation and mixing of seed particles, which are injected upstream of this turn. The air is then passed through a screen and honeycomb structure to reduce free-stream turbulence, followed by an annular converging-diverging nozzle, which accelerates the flow to a nominal design free-stream Mach number of 2.5 at the exit, with a 145-mm exit diameter.

The cylinder model used is a hollow steel tube with a threaded brass cap on the end, both of which have a constant diameter of 63.5 mm. The brass cap serves as the afterbody from which the flow separates, and terminates just past the nozzle exit. The weight of this model is cantilevered upstream of the nozzle entrance to prevent facility-induced disturbances from influencing the boundary layer profile at separation, to which the resulting near-wake flow field is highly sensitive [6,24]. The model runs through the center of the nozzle, and a lubricated slider plate, to which the nozzle is mounted, allows for translation of the nozzle position around the cylinder model. This translation was finely tuned such that the resulting flow field produced a statistically axisymmetric wake. A detailed schematic of the wind tunnel facility, as well as further details of wind tunnel operating conditions and procedures, including the model alignment procedures, can be found in Ref. [4].

Previous two-component PIV measurements of the flow conditions just upstream of separation found a boundary layer thickness of 0.11 base radii ($R_0 = 31.75$ mm) and maximum free-stream turbulence intensities of $0.008V_\infty$ and $0.004V_\infty$ in the axial and radial velocity components, respectively, where V_∞ is the free-stream velocity measured just upstream of flow separation ($V_\infty = 565$ m/s). The corresponding free-stream Mach number at the nozzle exit was measured to be 2.49. All data for this study were acquired across three separate runs of the wind tunnel, with an average stagnation pressure of 390 kPa and an average stagnation temperature of 287 K.

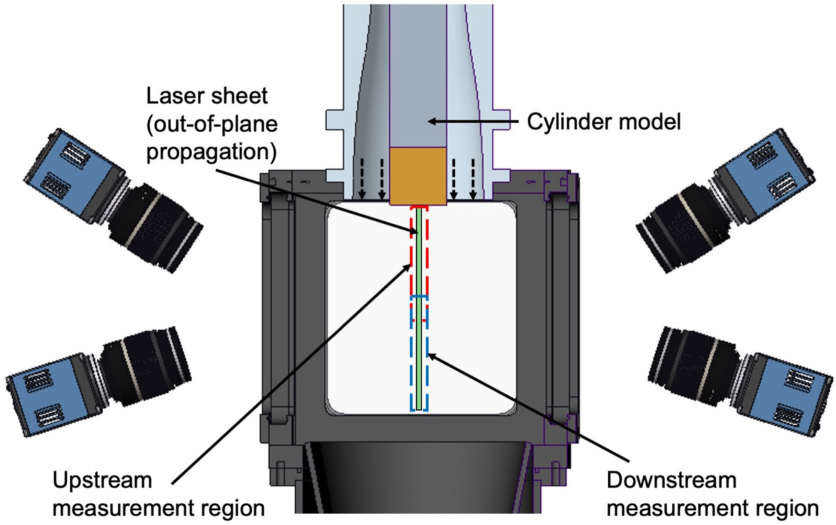

FIG. 2. Schematic of the SPIV experimental setup.

Additionally, the unit free-stream Reynolds number (i.e., $\mathrm{Re} = \rho V_\infty/\mu$) at separation was found to be $44 \times 10^6\ \mathrm{m}^{-1}$.

B. Stereoscopic PIV experiments

The primary diagnostic technique used in this study is stereoscopic PIV (SPIV), which measures all three components of velocity across a two-dimensional (2D) plane. In order to achieve a large field of view, two separate SPIV measurement regions were simultaneously acquired, and the resulting vector fields were merged during postprocessing to form one large composite field of view. The two separate measurement regions shared approximately 30% spatial overlap between them. These measurements were acquired along a plane coincident with the cylinder central axis, which constitutes a symmetry plane of the flow. A schematic of these SPIV experiments demonstrating the arrangement of the cameras relative to the cylinder model is shown in Fig. 2.

The four cameras used were all LaVision Imager sCMOS with sensor resolutions of 2560×2160 pixels and physical pixel sizes of $6.5\ \mu\mathrm{m}$. A single imaged seed particle typically occupied a 3×3 pixel region on the camera sensor, so pixel locking was not a concern during vector processing. Illumination of seed particles was provided with a New Wave Research SOLO PIV Nd:YAG laser, with 140 mJ/pulse and a temporal pulse separation of 583 ns, measured using a photodiode. Seeding for these experiments was provided by a ViCount 1300 aerosol generator, which provides an easily tunable, high-density stream of mineral-oil-based seed particles, with a mean particle diameter of 200 nm. This mean particle diameter is reported by the manufacturer and was confirmed via in-house experiments using the measured drag response across an oblique shock. Using this particle diameter, as well as the shear layer thickness at separation as the characteristic length scale, the maximum flow field Stokes number (i.e., the ratio of particle response time to eddy turnover time) was found to be 0.03 for these experiments, which is below the recommended value of 0.05 given by Samimy and Lele to identify accurate particle tracking [25]. Throughout much of the measurement region, as the characteristic length scales are spatially dependent, the Stokes number was less than 0.01.

Velocity field measurements were acquired at 15 Hz, which is several orders of magnitude slower than any characteristic timescales of the flow [26], so these measurements can be considered time-random snapshots of the flow. In total, $N = 3000$ planar velocity field measurements were acquired and processed. The resulting composite measurement region spans $0.06 \leqslant x/R_0 \leqslant 5.2$ in the streamwise direction, and $1.1R_0$ both above and below the central axis in the radial direction. A cylindrical coordinate system is used here to describe spatial locations (i.e., r and x for the radial and axial coordinates, respectively), with the origin defined as the center of the cylinder base. Additionally, velocities are presented in cylindrical components (i.e., V_r, V_θ, and V_x for radial, azimuthal, and axial components, respectively).

The composite vector field size is 284×125, with a uniform spacing of 0.577 mm between each vector. Cross-correlation windows to calculate velocities were 32×32 pixels in size with 50% spatial overlap, and the physical length of each window was approximately 1.1 mm. All processing was performed in the LaVision DaVis 8.4.0 software. A detailed uncertainty quantification was performed on these data, with the maximum mean-velocity uncertainties found to be approximately $0.02V_\infty$ for V_r, $0.08V_\infty$ for V_θ, and $0.03V_\infty$ for V_x. These maximum uncertainty values were calculated far upstream in the shear layer near separation, and the measurement uncertainties decayed rapidly further downstream. Further details about these experiments including image-processing parameters, calibration procedures, and the full results of the uncertainty quantification process are given in Ref. [4].

C. Proper orthogonal decomposition

In this study, proper orthogonal decomposition (POD) was used to decompose the turbulent flow field into a set of orthogonal basis functions (i.e., modes). The method used here is the space-only, so-called snapshot method, first proposed by Sirovich [19]. In this method, each instantaneous measurement plane is considered a snapshot of the flow, with no temporal correlation existing between any two snapshots. By construction of the method, N snapshots will produce N spatially dependent modes (here $N = 3000$), which have been optimally decomposed for a turbulent kinetic energy (TKE) basis [27]. The turbulent energy contained within each mode can also be shown for this method to be directly proportional to the corresponding eigenvalue of each mode, so the total set of modes can be sorted into descending order of their fractional contribution toward the total TKE. To isolate turbulent motions within these modes, the POD was performed on the velocity fluctuations (i.e., V_r', V_θ', and V_x'), which are defined by the standard Reynolds decomposition (i.e., $V = \langle V \rangle + V'$).

It should be noted that the current flow is highly compressible (as will be demonstrated in the next section) and thus exhibits significant density gradients. A true measure of the local TKE would be weighted by the local fluid density, but without having knowledge of the instantaneous density fields corresponding to each velocity field snapshot, which is not available in the current work, the true measure of TKE is not obtainable. Van Gent *et al.* [28] discuss the feasibility of using PIV velocity field measurements to obtain time-averaged pressure and/or density fields in a compressible flow, but they note that determination of instantaneous pressure and/or density fields without having time-resolved three-dimensional velocity field measurements is infeasible. As a result, the POD modes resulting from this analysis are not truly indicative of a spatial map of TKE, as there exists an energy bias in the POD analysis toward the lower-density flow regions. However, in the current work, the key results are derived from conditional sorting and averaging of the velocity field snapshots themselves, with the POD modes simply being used as identifiers of specific snapshots of interest (i.e., the interpretation of flow physics results is not derived from the mode shapes themselves). Thus, this inherent energy bias in the current POD analysis does influence the resulting eigenspectrum of mode shapes, but it does not influence the conclusions drawn in this work.

The POD algorithm and implementation for the current work were inspired by the method of Meyer *et al.* [29]. In this method, the ith snapshot is oriented as a column vector (v^i), with M spatial locations contained within that snapshot. This column vector is constructed by indexing between locations 1 to M for each separate velocity component, and stacking all three components of velocity on top of one another (i.e., each column vector, v^i, is $3M \times 1$ in size). Each separate snapshot is then stacked together to form the matrix U, which has a size of $3M \times N$, and is given by Eq. (1).

$$U = [v^1 \quad v^2 \quad \dots \quad v^N] = \begin{bmatrix} V'^1_{r\,1} & V'^2_{r\,1} & \dots & V'^N_{r\,1} \\ \vdots & \vdots & \ddots & \vdots \\ V'^1_{r\,M} & V'^2_{r\,M} & \dots & V'^N_{r\,M} \\ V'^1_{\theta\,1} & V'^2_{\theta\,1} & \dots & V'^N_{\theta\,1} \\ \vdots & \vdots & \ddots & \vdots \\ V'^1_{\theta\,M} & V'^2_{\theta\,M} & \dots & V'^N_{\theta\,M} \\ V'^1_{x\,1} & V'^2_{x\,1} & \dots & V'^N_{x\,1} \\ \vdots & \vdots & \ddots & \vdots \\ V'^1_{x\,M} & V'^2_{x\,M} & \dots & V'^N_{x\,M} \end{bmatrix}. \tag{1}$$

The autocovariance matrix, C, is then constructed by Eq. (2):

$$C = \frac{1}{N} U^{\mathsf{T}} U. \tag{2}$$

The decomposition is then performed by solving the eigenvalue problem for matrix C, where the ith eigenvalue and eigenvector are given by λ^i and D^i, respectively, and are found by solving Eq. (3). This construction of C produces N total eigenvectors:

$$CD^i = \lambda^i D^i. \tag{3}$$

The eigenvectors then make up a basis for the construction of each POD mode, where the ith normalized POD mode (Φ^i) is constructed by Eq. (4). The ||...|| operator in Eq. (4) represents the discrete $L-2$ norm:

$$\Phi^i = \frac{\sum_{k=1}^{N} D^i_k v^k}{\left\| \sum_{k=1}^{N} D^i_k v^k \right\|}. \tag{4}$$

Additionally, the fractional TKE contained within any Φ^i mode is directly proportional to the magnitude of the corresponding eigenvalue for that mode, λ^i. Therefore, the modes can be reordered in descending order of fractional energy contribution toward the total TKE by Eq. (5):

$$\lambda^1(\Phi^1) > \lambda^2(\Phi^2) > \lambda^3(\Phi^3) > \cdots > \lambda^N(\Phi^N). \tag{5}$$

By this construction, each mode is $3M \times 1$ in size, and the projection of each mode onto a coordinate direction (i.e., Φ^i_r for the radial component of the ith mode) is found by simply extracting the corresponding components of the Φ^i vector, which is given by Eqs. (6) and (7):

$$[\Phi^1 \quad \Phi^2 \quad \dots \quad \Phi^N] = \begin{bmatrix} \phi_{r\,1}^{\,1} & \phi_{r\,1}^{\,2} & \dots & \phi_{r\,1}^{\,N} \\ \vdots & \vdots & \ddots & \vdots \\ \phi_{r\,M}^{\,1} & \phi_{r\,M}^{\,2} & \dots & \phi_{r\,M}^{\,N} \\ \phi_{\theta\,1}^{\,1} & \phi_{\theta\,1}^{\,2} & \dots & \phi_{\theta\,1}^{\,N} \\ \vdots & \vdots & \ddots & \vdots \\ \phi_{\theta\,M}^{\,1} & \phi_{\theta\,M}^{\,2} & \dots & \phi_{\theta\,M}^{\,N} \\ \phi_{x\,1}^{\,1} & \phi_{x\,1}^{\,2} & \dots & \phi_{x\,1}^{\,N} \\ \vdots & \vdots & \ddots & \vdots \\ \phi_{x\,M}^{\,1} & \phi_{x\,M}^{\,2} & \dots & \phi_{x\,M}^{\,N} \end{bmatrix}, \tag{6}$$

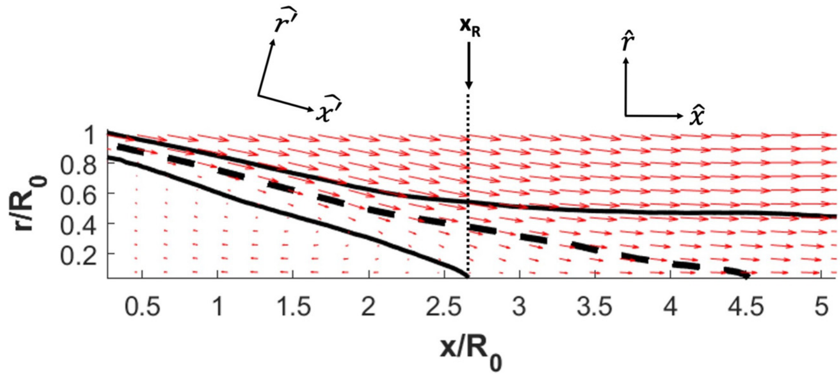

FIG. 3. Mean flow vector plot demonstrating the primed and global coordinate system definitions. The vectors are sampled to display only one out of every five in both directions. Solid contours represent shear layer boundaries, and the dashed contour represents the mean sonic line.

$$\Phi_r^i = \begin{bmatrix} \phi_{r1}^{\,i} \\ \vdots \\ \phi_{rM}^{\,i} \end{bmatrix}, \quad \Phi_\theta^i = \begin{bmatrix} \phi_{\theta 1}^{\,i} \\ \vdots \\ \phi_{\theta M}^{\,i} \end{bmatrix}, \quad \Phi_x^i = \begin{bmatrix} \phi_{x1}^{\,i} \\ \vdots \\ \phi_{xM}^{\,i} \end{bmatrix}. \tag{7}$$

The time-dependent amplitude coefficients, which will simply be referred to as POD coefficients, can then be constructed by projecting the normalized modes onto a snapshot. The POD coefficient corresponding to the ith mode and the jth snapshot (a_i^j) is given by Eq. (8):

$$a_i^j = \Phi^{i\mathsf{T}} v^j. \tag{8}$$

Finally, because these POD modes constitute an orthogonal and complete set of basis functions for the flow, any jth snapshot can be fully reconstructed by Eq. (9):

$$v^j = \sum_{i=1}^{N} a_i^j \Phi^i. \tag{9}$$

III. SHEAR LAYER GROWTH AND COMPRESSIBILITY

The time-averaged behavior of the shear layer in this flow is first investigated by examining the shear layer growth. The metric used here to define the shear layer thickness is the vorticity thickness, or the "velocity-profile maximum-slope" thickness [7], which is commonly used to characterize the growth of separated shear layers [9,30]. The definition of the vorticity thickness is given by Eq. (10):

$$\delta_\omega(x') = \frac{U_1 - U_2}{\max\left(\frac{\partial \langle V_{x'} \rangle}{\partial r'}(x', r')\right)}. \tag{10}$$

In this flow, the separated shear layer is turned radially inward by the expansion fan at separation. Therefore, to analyze the spatial growth of the shear layer, the mean flow data upstream of the reattachment point (x_R) were rotated into the $x' - r'$ coordinate system, the definition of which is given by Fig. 3. In this figure, the solid contours represent the shear layer boundaries, the dashed contour represents the mean sonic line ($M = 1$), and only one out of every five vectors in each direction was plotted (i.e., only one out of every 25 total vectors is shown). The turning angle of the primed coordinate system relative to the global coordinates system is 14.7°, which was found to be the mean flow orientation in the center of the shear layer.

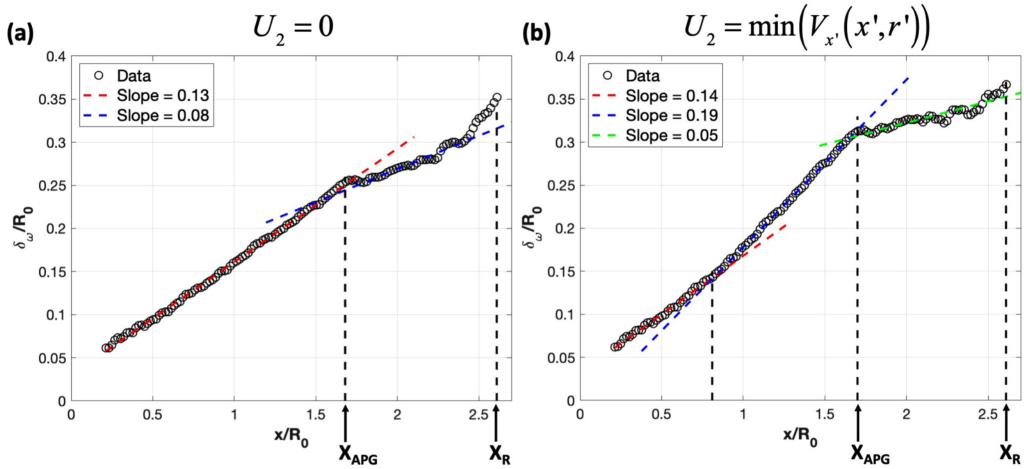

FIG. 4. (a) Shear layer vorticity growth rate with $U_2 = 0$ and (b) vorticity growth with $U_2(x') = \min(V_{x'})$ along traverses in the r' direction.

In Eq. (10), $U_1 = 1.06V_\infty$, which is the free-stream velocity after being accelerated by the expansion fan. Two separate choices of U_2, however, are examined here. The first definition, $U_2 = 0$, fixes the numerator of Eq. (10) as a constant, which models the growth of the shear layer to be purely a function of the streamwise rate of decay of the maximum shearing [i.e., the denominator of Eq. (10)]. In this definition, a rapid decay of maximum shearing implies a rapid spreading of the shear layer, which in turn drives a high vorticity growth rate. The second definition has U_2 equal to the minimum value of $V_{x'}$ along an r' traverse, which makes this definition of vorticity growth dependent on the local reverse flow velocity as well as the streamwise decay of maximum shearing. The vorticity thickness plots using both of these U_2 definitions are shown in Fig. 4. Using Eq. (10), the vorticity thickness was found at each x' location by taking a traverse along the r' coordinate, which is orthogonal to the direction of mean shear layer convection. This x' location was then mapped back to the global x coordinate for plotting, at the r' location corresponding to the center of the shear layer.

In Fig. 4(a), there are a few distinct regions in the shear layer growth. From the upstream-most data point to approximately $x/R_0 = 1.7$, the shear layer is characterized by a region of very uniform linear growth, with a slope of 0.13. This trend is similar to unseparated free shear layers, which exhibit a linear growth for both incompressible and compressible cases [31]. The sharp dropoff in growth rate after this point is attributed to the onset of the adverse pressure gradient (APG) associated with flow-field recompression. Although there are not pressure measurements in this region to confirm the onset of the APG, this location is consistent with the onset of mean streamline curvature in the velocity field data, as well as visualizations of shocklets in schlieren images of this flow. Throughout the APG region of the flow, which extends between approximately $1.7 < x/R_0 < 3.75$, the shear layer encounters so-called extra strain rates in addition to the mean shearing, such as bulk compression and concave streamline curvature, as well as radial streamline convergence near reattachment. These extra strain rates have been studied in high-speed boundary layers, with bulk compression and concave streamline curvature having been shown to further destabilize the flow and increase turbulent activity, while radial streamline convergence has been shown to have a stabilizing influence on the flow [32–34]. These effects are consistent with the turbulence in this flow, as rapid increases in TKE have been demonstrated in the shear layer downstream of the onset of the APG, with reductions in the TKE occurring as the shear layer approaches reattachment [4,12].

In the context of vorticity thickness, however, the APG induces this reduction in growth rate as the flow is turned into itself, inhibiting the spread of the high-shear region of the shear layer, and reducing the streamwise decay of maximum shearing. Further downstream near reattachment, however, the influence of the streamline convergence effect becomes more dominant and drives a rapid spreading of the shear layer, which in turn drives a rapid streamwise decay in the maximum shearing. This results in a large jump in the vorticity growth rate just upstream of reattachment. In comparison to previous results for compressible, unseparated, two-stream shear layers; however, this result is counterintuitive. A recent study by Kim *et al.* [31] demonstrated that reduced shear layer TKE directly correlated with reduced shear layer growth rates across a wide range of compressibility levels. However, in the shear layer of this flow, in the presence of the extra strain rates, the increased TKE region correlates with reduced shear layer growth, and the reduced TKE region near reattachment correlates with increased shear layer growth. This is indicative of stark differences in the turbulence mechanisms, such as entrainment, which drive the growth of the shear layers in these flows. This is perhaps due to the increased importance of coherent large-scale structures along the shear layer boundaries in this flow. In a DNS study of unseparated shear layers with varying compressibility levels, Jahanbakhsi *et al.* [21] found that small-scale "nibbling" mechanisms dominated the entrained mass flow across the turbulent/nonturbulent interface separating the viscous shear layer fluid from the inviscid free stream for both incompressible and compressible cases. In unseparated shear layers, both the low-speed and high-speed boundaries separate it from inviscid free-stream fluid, but in the current separated flow, the low-speed shear-layer boundary borders a highly turbulent recirculation region. Previous work by the current authors [35] has demonstrated the prevalence of coherent large-scale turbulent structures along this low-speed shear-layer boundary, and it is quite probable that they significantly influence the shear-layer growth characteristics, and produce stark differences in the growth mechanisms between separated and unseparated shear layers.

The second definition of vorticity thickness [Fig. 4(b)], displays features similar to Fig. 4(a), but the upstream portion of the shear layer is now characterized by two separate regions of linear growth, with growth rates of 0.14 and 0.19, respectively. This definition also experiences a drop-off in growth rate at the onset of the APG, but the drop-off is more pronounced in this definition, reducing to 0.05 versus 0.08 for Fig. 4(a). A DNS study of this flow by Sandberg [6] found trends in vorticity growth rate similar to those of Fig. 4(a), while the trends in Fig. 4(b) compare well to a DES study by Simon *et al.* [9], who also observed these two separate regions of linear growth in the upstream portions of the shear layer. Although the general trends were similar in both cases, the actual computed growth rates were quite different from the current experimental data, as Sandberg found a growth rate in the single linear region of 0.25 and Simon *et al.* found growth rates in the two linear regions to be 0.25 and 0.38, respectively.

In addition to growth rates, an important factor that influences shear layer development is the amount of compressibility present, which is typically characterized by the convective Mach number, M_c [36], and is given by Eq. (11). In this definition, c_1 is the local speed of sound at U_1, and c_2 is the local speed of sound at U_2:

$$M_c = \frac{U_1 - U_2}{c_1 + c_2}. \tag{11}$$

Using the definition of U_2 for Fig. 4(a), M_c takes on a constant value of approximately 1.1 throughout the entire shear layer. However, this parameter describes the Mach number of the flow in the convective frame of reference of the local large-scale structures, so this parameter is more aptly defined here using the second definition of U_2, which was used in Fig. 4(b). This gives M_c as a function of x within the shear layer, which is shown by Fig. 5.

Figure 5 demonstrates that, throughout the entire streamwise extent of the shear layer, M_c is greater than unity, which indicates very high levels of compressibility. Near the mean onset location of the APG, the local M_c peaks at a value of 1.38 and then decays to a value of 1.17 at the reattachment location.

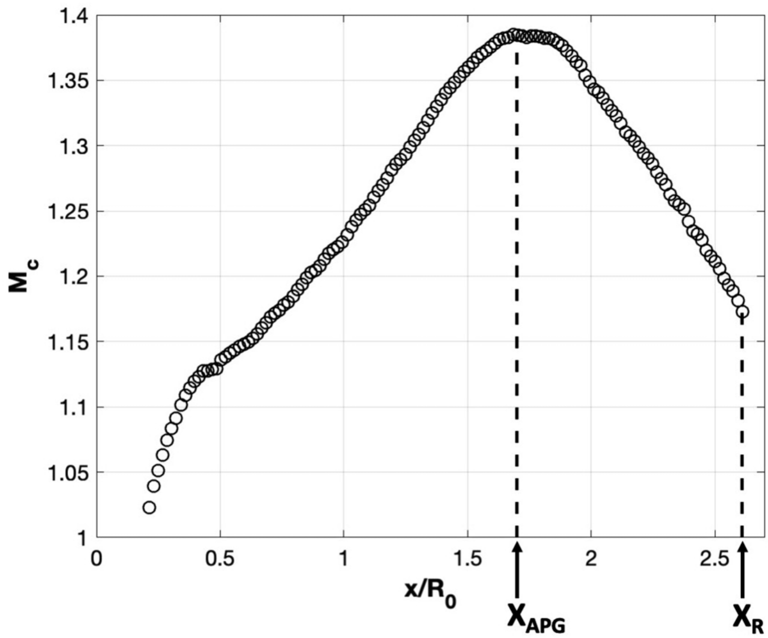

FIG. 5. Streamwise evolution of convective Mach number within the separated shear layer.

IV. PROPER ORTHOGONAL DECOMPOSITION ANALYSIS

A. POD modes and energy convergence

The full ensemble of SPIV data ($N = 3000$ snapshots) was decomposed into POD modes using the method outlined in Sec. II C. As mentioned previously, the fractional TKE contained within a given mode can be extracted from the magnitude of the eigenvalue corresponding to that mode. The modes were sorted in order of descending energy, and the energy convergence as a function of mode number is plotted in Fig. 6. Figure 6(a) shows the fractional energy contained within each of the 25 highest energy-containing modes on a linear scale, Fig. 6(b) shows the fractional energy for all modes on a log-log scale, and Fig. 6(c) shows the cumulative energy convergence for all modes on a semilog scale.

The highest energy-containing mode only accounts for 7.5% of the flow TKE, with the energy spectrum decaying exponentially with increasing mode number. In Fig. 6(b), there is a linearly

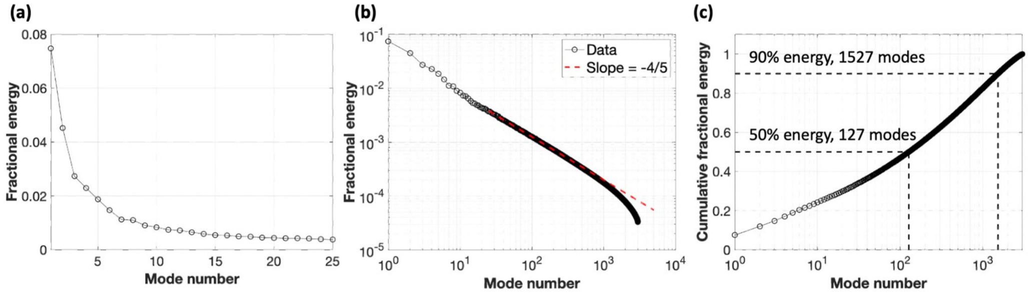

FIG. 6. (a) Fractional energy vs mode number for the first 25 modes (linear scale), (b) fractional energy vs mode number for all modes (log-log scale), and (c) cumulative energy vs mode number across all modes (semilog scale).

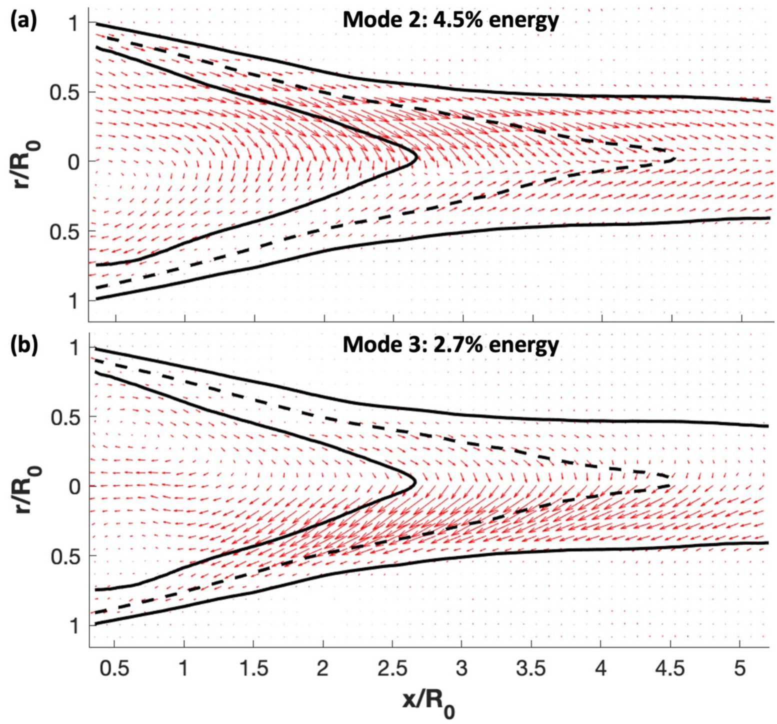

FIG. 7. (a) POD mode 2 and (b) POD mode 3. Vectors are depicted by Φ_r and Φ_x for each mode, and are defined by Eq. (7). Solid contours represent shear layer boundaries and the dashed contour represents the mean sonic line.

decaying region in the fractional energy plot (on a log-log scale) between approximately mode numbers 20 and 800, wherein the decay follows a uniform slope of $-4/5$. This could be indicative of an inertial subrange within the data, similar to those identified using the eigenvalue spectra in inhomogeneous channel flows by Knight and Sirovich [37]. Figure 6(c) demonstrates that it takes 127 modes (or 4.2% of the total modes) to capture 50% of the TKE, and 1527 modes (or 50.9% of the total modes) to capture 90% of the TKE. This large number of modes required to achieve these energy convergence benchmarks makes POD an impractical tool for constructing a reduced-order computational model of this flow. This poor energy convergence is not unexpected, however, as the high Re and high levels of compressibility distribute the turbulent energy across a very broad spectrum of temporal and spatial scales. This, combined with the many different complex subregions of this flow, makes it difficult for the POD method to decompose large fractions of the total TKE into singular modal representations. Additionally, this POD energy convergence compares quite well to that of an LES study of this same flow by Das and De [38], as well as that of supersonic planar base flows by Humble *et al.* [3].

Projecting a POD mode onto a set of coordinate directions [Eq. (7)] allows for examination of the dynamics identified by that mode. The highest energy-containing mode, representing 7.5% of the TKE, was found to be dominated by out-of-plane azimuthal velocity fluctuations in the shear layer and recirculation region, with essentially no in-plane turbulent motion. However, for the present study, the second and third POD modes were found to exhibit the most interesting dynamics, with these two modes representing 4.5% and 2.7% of the total flow TKE, respectively. Vector plots of the in-plane motions depicted by these two modes are shown in Fig. 7. Additionally, a complete description of the dynamics of a given mode requires its corresponding distribution of POD coefficients [defined by Eq. (8)], which identify how strongly and in what direction that mode

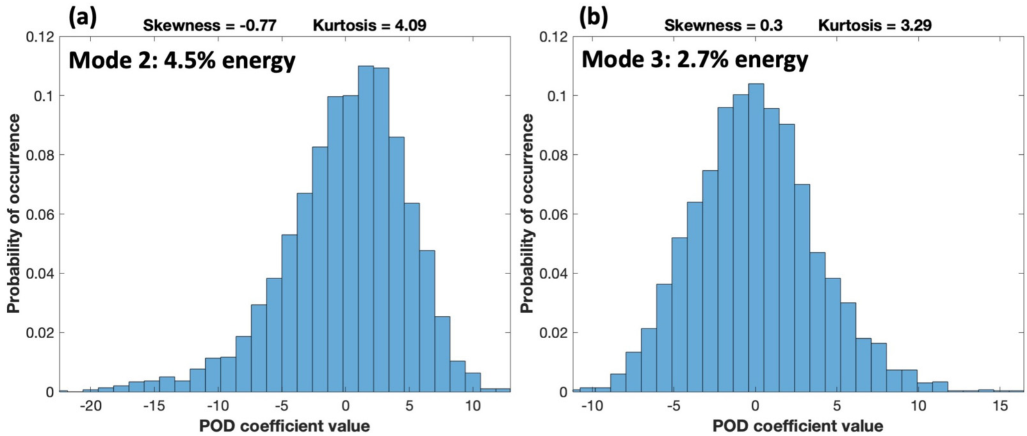

FIG. 8. (a) POD coefficient distribution for mode 2 and (b) POD coefficient distribution for mode 3.

is acting during a given snapshot of the flow. The corresponding distributions of POD coefficients for modes 2 and 3, presented as discrete probability density functions, are shown in Fig. 8.

The two modes depicted in Fig. 7 appear to identify dynamics similar to one another, but in the two separate shear layers. Mode 2 demonstrates a large velocity fluctuation in the positive axial and negative radial directions (i.e., $V_x' > 0$ and $V_r' < 0$), which are defined as Q4 events, to use the terminology of turbulent quadrant analysis [39], as this velocity fluctuation direction would exist in the fourth quadrant on a plot of V_r' versus V_x'. This motion exists throughout much of the subsonic portions of the upper shear layer, and extends past reattachment and into the trailing wake. This motion is limited to the upper shear layer in mode 2, with the dynamics of the lower shear layer appearing uninfluenced by this mode. This is directly opposite, however, for mode 3, as the lower shear layer now exhibits similar dynamics, while the upper shear layer exhibits no turbulent motion. Mode 3 demonstrates negative axial and positive radial velocity fluctuations (i.e., $V_x' < 0$ and $V_r' > 0$), which are defined as Q2 events. However, the direction in which the mode acts during a given snapshot depends on the sign of the corresponding POD coefficient. For example, if a mode 2 coefficient corresponding to a particular snapshot were positive, then mode 2 acts during that snapshot in the direction depicted by the vectors in Fig. 7(a). Alternatively, if the coefficient for a snapshot were negative, then the vectors of that mode are reversed for that snapshot. Q2 and Q4 events are directionally opposite to one another, so in the context of mode 2 in Fig. 7(a), positive POD coefficients depict Q4 directional turbulent events, and negative POD coefficients depict Q2 turbulent events.

The histograms of POD coefficients in Fig. 8 both depict skewed distributions. Mode 2 is skewed toward negative values, which indicates Q2 turbulent events in the upper shear layer, and mode 3 is skewed toward positive values, which also indicates Q2 turbulent events in the lower shear layer. Therefore, it appears that both of these modes demonstrate similar dynamics to one another, but in each of the two shear layers separately. In reality, the shear layer in this flow is a continuous 3D conical region, but it is depicted as two separate shear layers here in this planar representation.

B. Conditional statistics

Rather than using the space-only POD analysis to interpret the physical coherent motions of the flow from the POD modes themselves, which has recently been criticized in Refs. [40–44], this work will instead investigate the flow dynamics through conditional sorting and averaging of the velocity field snapshots, utilizing the POD coefficient distributions as sorting criteria.

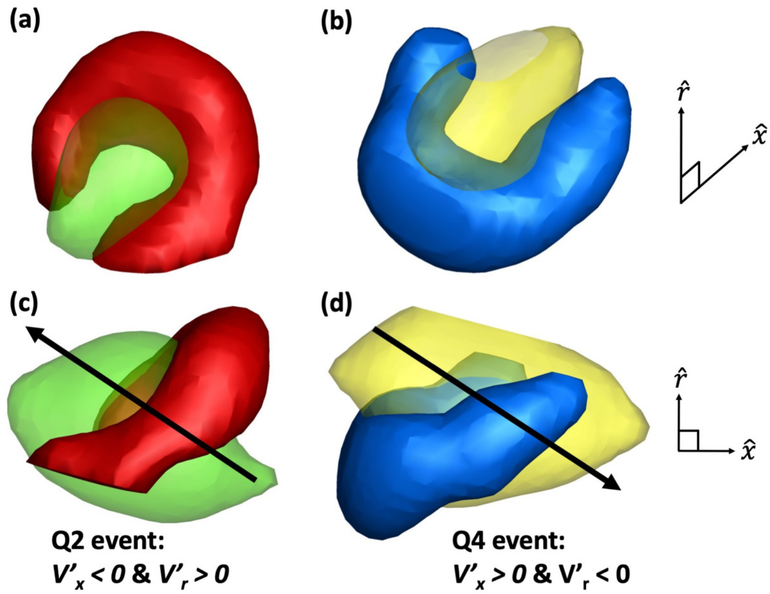

FIG. 9. (a) Conditionally resolved upright hairpin (red) inducing a strong Q2 event (green), (b) conditionally resolved inverted hairpin (blue) inducing a strong Q4 event (yellow), (c) side view of panel (a), and (d) side view of panel (b). These results are from previous work by the authors using TPIV measurements of the same flow [35].

The Q2 and Q4 motions identified by modes 2 and 3 in Fig. 7 were demonstrated in recent work by the authors to be the result of coherent upright and inverted hairpin vortex structures [35]. In this study, tomographic PIV (TPIV) measurements of this same flow field were acquired, which provide the full volumetric extent of the 3D turbulent structures, and linear stochastic estimation [45] was used to conditionally average the velocity fields and provide robust statistical evidence of the frequent existence of these structures throughout the shear layer and trailing wake of this flow. These structures were demonstrated to exhibit a concentrated shearing mechanism between their heads and legs, such as has been typically demonstrated for hairpin vortices in wall-bounded flows [46,47], which causes them to induce strong velocity fluctuations in a consistent direction. It was shown in this previous work that upright hairpins induce strong and consistent velocity fluctuations in the Q2 direction, while inverted hairpins induced strong and consistent velocity fluctuations in the Q4 direction. In this context, an inverted hairpin vortex is dynamically similar but topologically inverted compared to an upright hairpin. They form via similar instability mechanisms as the upright hairpins, and exhibit similar features, but can only form in free shear flows without a wall boundary constraint [48]. Conditionally averaged depictions of these structures from this previous work are demonstrated in Fig. 9. In this figure, the upright and inverted hairpin structures (the red and blue isocontours, respectively) are educed by the swirling strength criterion [49], which was computed on the conditionally averaged 3D TPIV velocity fields. Additionally, the concentrated Q2 and Q4 events in 3D space are depicted in this figure by the green and yellow translucent contours, respectively, which are both inherently defined by a large constant value of $V_r'V_x' < 0$. Furthermore, these structures were resolved along the low-speed shear layer boundary at approximately $x/R_0 = 1.8$.

This previous work [35] also demonstrated that both of these types of structures were the dominant contributors to the kinematic Reynolds shear stress and TKE of this flow, especially in the subsonic portions of the shear layer near reattachment, where the POD modes of Fig. 7 demonstrate the strongest Q2 and Q4 activity. Therefore, the authors postulate that POD modes 2

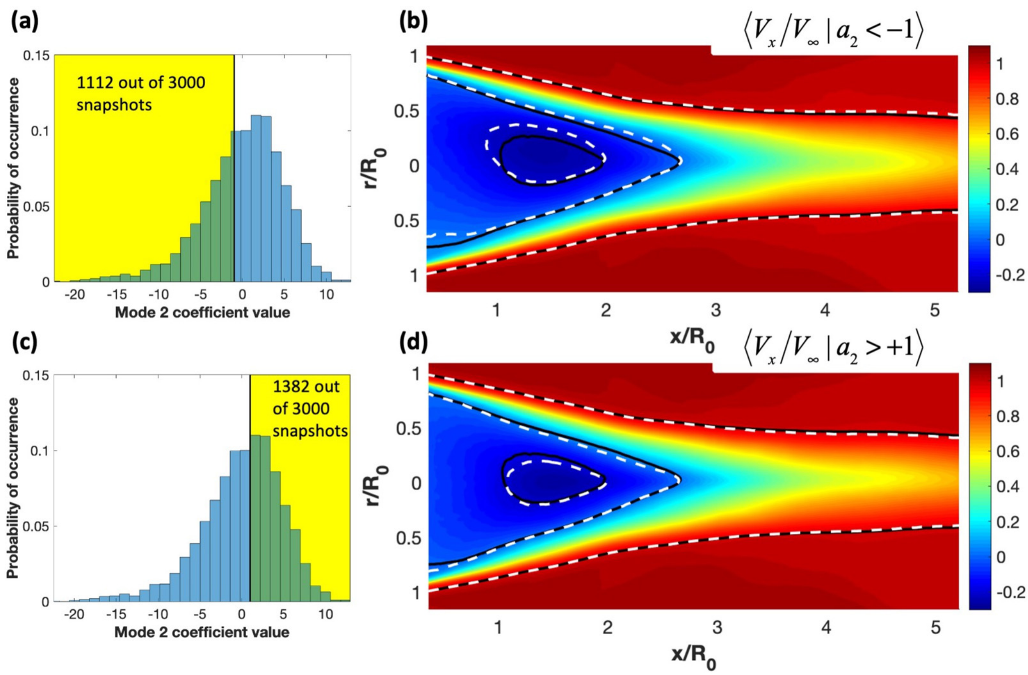

FIG. 10. (a) Visualization of $a_2 < -1$ condition, (b) conditional average of V_x/V_∞ given that $a_2 < -1$, (c) visualization of $a_2 > +1$ condition, and (d) conditional average of V_x/V_∞ given that $a_2 > +1$. Contour lines represent the shear layer boundaries and the constant value $V_x/V_\infty = -0.2$ contour. Solid black contours depict the unconditional mean flow, and dashed white contours represent the same features of the conditional flow.

and 3 of the current work depict high-energy spatial correlations of velocity fluctuations induced by these coherent structures, and thus act as identifiers of velocity field snapshots that contain these structures.

As mentioned previously, the POD coefficients were used to sort the ensemble of snapshots into conditional subsets. This was done here by defining a minimum magnitude value, and extracting all snapshots with a corresponding POD coefficient whose magnitude exceeded that value. This is done on both sides of the POD coefficient distribution (i.e., for both strong positive and negative values). Conditional averages of the mean axial velocity, sorted based on $a_2 < -1$ and $a_2 > +1$, are shown in Fig. 10. In this figure, the solid contour lines represent both the shear layer boundaries from previous figures, as well as the constant-valued contour of $V_x/V_\infty = -0.2$, which is intended to represent the bulk region of relatively high-speed recirculated fluid. The solid black contours represent the unconditional mean flow depiction of these features, and the dashed white contours represent the conditionally resolved features. Additionally, the histograms in this figure depict the subset of snapshots used to derive the corresponding conditional flow field.

Figure 10 clearly demonstrates the influence of mode 2 on the mean development of the shear layers in this flow. For snapshots corresponding to $a_2 < -1$, which are depicted by the yellow portion of the histogram in Fig. 10(a), the mean growth rate of the upper shear layer is reduced when compared to the unconditional flow, and the mean reattachment point shifts slightly downstream and above the central axis. This is identified by examining the differences in the solid black and dashed white contours of the inner shear layer boundary in Fig. 10(b). This change in growth rate is accompanied by a shift in the bulk region of recirculated fluid toward this upper shear layer. Both of these results are indicative of the mean mass entrainment/detrainment rates between the shear

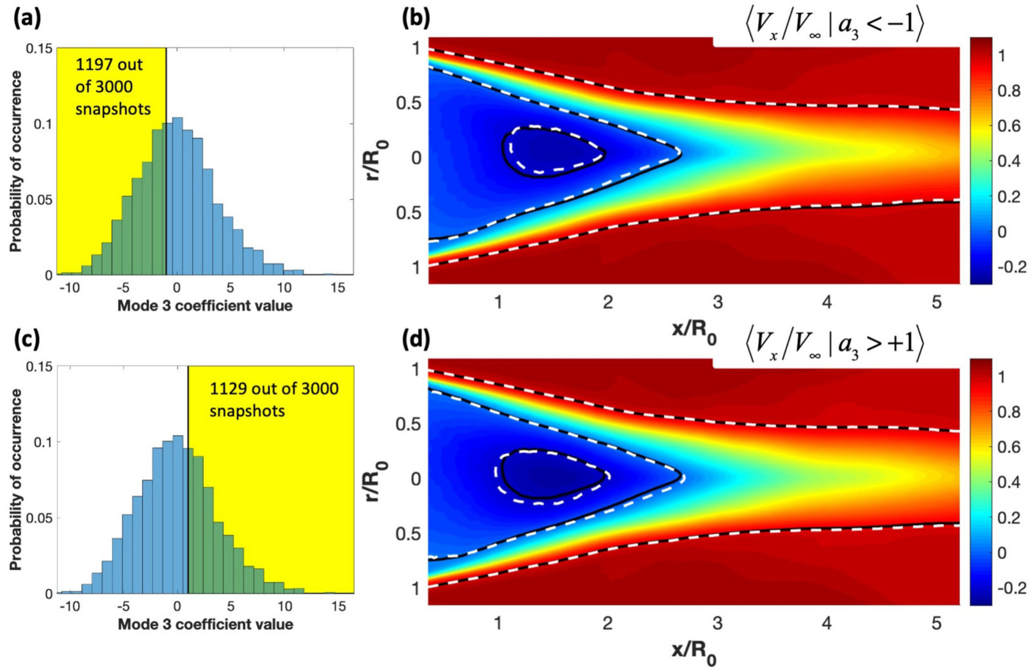

FIG. 11. (a) Visualization of $a_3 < -1$ condition, (b) conditional average of V_x/V_∞ given that $a_3 < -1$, (c) visualization of $a_3 > +1$ condition, and (d) conditional average of V_x/V_∞ given that $a_3 > +1$. Contour lines represent the shear layer boundaries and the constant value $V_x/V_\infty = -0.2$ contour. Solid black contours depict the unconditional mean flow, and dashed white contours represent the same features of the conditional flow.

layer and recirculation region being reduced for this conditionally resolved flow, particularly in the downstream portions of the shear layer, where the turbulent energy is highest.

Examining the conditional average for the other side of the POD coefficient histogram [Fig. 10(c)], Fig. 10(d) depicts the conditional flow, now conditioned on $a_2 > +1$. The conditional motions of Fig. 10(d) are opposite that of Fig. 10(b), in that the upper shear layer now exhibits a higher mean growth rate, and the bulk region of recirculating fluid shifts away from the upper shear layer. This is now indicative of the mean mass entrainment/detrainment rates between the shear layer and recirculation region being increased in the upper shear layer. For both conditional cases [Figs. 10(b) and 10(d)], the contours defining the lower shear layer do not change between the unconditional case and either conditional case. The only exception is far upstream in the lower shear layer, but this is believed to be caused by measurement noise, as the far upstream regions of the shear layer were found to have significantly higher experimental uncertainties than the downstream portions [4]. This higher uncertainty further upstream primarily stems from laser reflections from the cylinder surface, in addition to higher particle lag.

The same conditional averaging scheme was also performed for the coefficient distribution of mode 3, with the results shown in Fig. 11. The conditional averages of the flow for this mode demonstrate the same dynamics as mode 2, except now for the lower shear layer. The lower shear layer growth rate is increased, with the bulk region of recirculated fluid shifting away from the lower shear layer for $a_3 < -1$ [Fig. 11(b)], and the lower shear layer growth rate is decreased, with the bulk-region of recirculated fluid shifting toward the lower shear layer for $a_3 > +1$ [Fig. 11(d)]. Additionally, in both cases, the upper shear layer does not change between the unconditional and two conditional cases. Therefore, from Figs. 10 and 11, it seems that Q2 motions in the shear

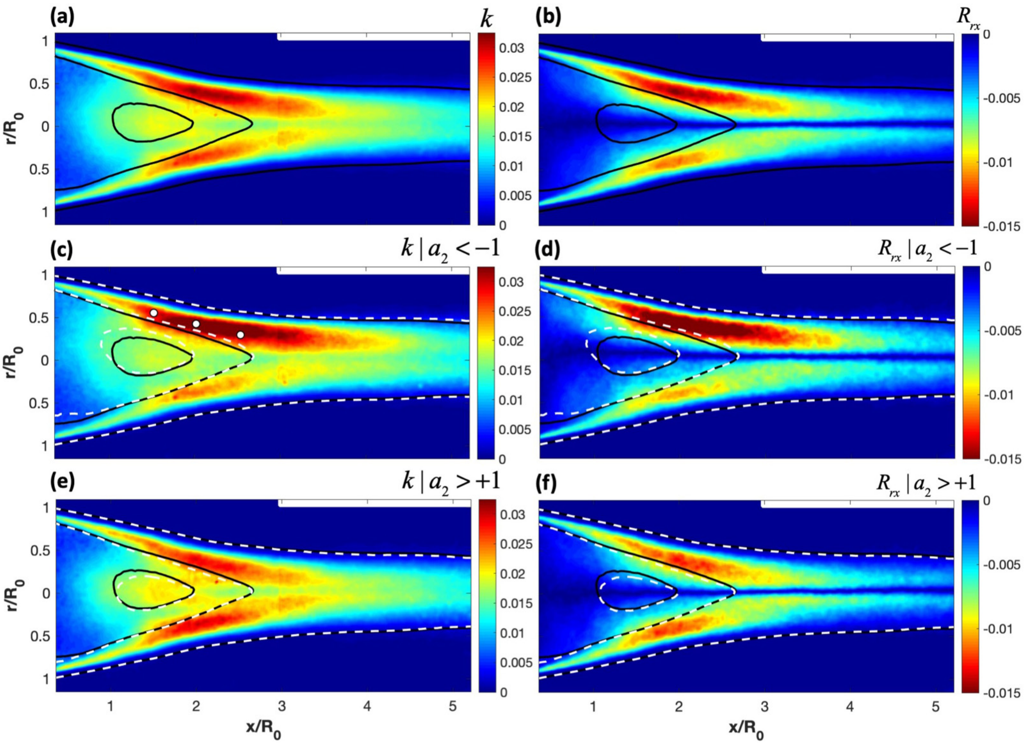

FIG. 12. (a) Unconditional TKE, (b) unconditional R_{rx}, (c) conditional TKE given $a_2 < -1$, (d) conditional R_{rx} given $a_2 < -1$, (e) conditional TKE given $a_2 > +1$, and (f) conditional R_{rx} given $a_2 > +1$. Contour lines represent the same features as Fig. 10. White dots in panel (c) represent locations of scatter plots in Fig. 13.

layer correlate with reduced shear layer growth rates, and thus a reduction in mean shear layer entrainment/detrainment rates, and vice versa for Q4 motions. Note that positive a_2 values depict Q4 motions in the upper shear layer of mode two (Fig. 7), and negative values of a_2 depict Q2 motions. Also, for mode 3, positive values of a_3 depict Q2 motions in the lower shear layer, and negative values of a_3 depict Q4 motions.

To further investigate the influence of these Q2 and Q4 motions in the shear layer, the primary kinematic Reynolds shear stress and TKE for the unconditional flow, as well as for the conditions of $a_2 < -1$ and $a_2 > +1$, are shown in Fig. 12. The kinematic Reynolds stress tensor is defined by Eq. (12), and the TKE is defined by Eq. (13). Additionally, as the previous figures have demonstrated that the motions of modes 2 and 3 were essentially the same, just differentiated between the upper and lower shear layers, only the conditional statistics for mode 2 are shown in Fig. 12, for succinctness:

$$R_{ij} = \langle V_i' V_j' \rangle, \tag{12}$$

$$k = \tfrac{1}{2}(R_{rr} + R_{\theta\theta} + R_{xx}). \tag{13}$$

Figure 12(a) demonstrates that the TKE of the unconditional flow is dominant within the downstream portions of the shear layer near the low-speed boundary. Aside from the zero values of R_{rx} along the central axis, which is enforced by the flow symmetry constraint, the unconditional R_{rx} in Fig. 12(b) is essentially a mirror image of the TKE in Fig. 12(a). This shows that regions of high TKE correlate with regions of high shear stress, which were both shown in previous work by the authors [35] to be dominated by the previously described upright and inverted hairpin vortices throughout this flow. In this previous work, it was demonstrated that the upright hairpin vortices had a slight dominance in energy contribution over the inverted hairpins, as the upright hairpins were prevalent throughout the entire transverse extent of the shear layer (i.e., both subsonic and supersonic regions), while the inverted hairpins were found to only exist in the lower-speed subsonic regions of the shear layer.

The condition of $a_2 < -1$, which identifies Q2 fluctuations in the upper shear layer, demonstrates a significant increase in TKE and R_{rx} throughout the high-energy regions of the upper shear layer and trailing wake [Figs. 12(c) and 12(d)]. Alternately, the positive side of the POD coefficient distribution, which identifies Q4 fluctuations in the upper shear layer, demonstrates slight decreases in the TKE and R_{rx} contours compared to the unconditional plots [Figs. 12(e) and 12(f)]. However, the magnitude of the decreases in these values between the unconditional and $a_2 > +1$ contours are significantly less than the magnitude of the increases between the unconditional and the $a_2 < -1$ contours. Additionally, it should be noted that both the unconditional TKE and the unconditional kinematic shear stress plots of Figs. 12(a) and 12(b) display an asymmetry between the upper and lower shear layers. This is most likely a result of a very small misalignment (beyond the translational resolution of the alignment mechanism in the current wind tunnel facility) of the cylinder model relative to the free-stream flow, to which second-order turbulence statistics (such as the TKE) are highly sensitive. This slight asymmetry is believed to be the reason for the difference in the energy fraction between modes 2 and 3, even though they represent the same dynamics (i.e., mode 2 represents the Q2 and Q4 dynamics in the upper shear layer with 4.5% of the TKE fraction, while mode 3 represents the same Q2 and Q4 motions in the lower shear layer with only 2.7% of the TKE fraction).

To further demonstrate that POD mode 2 acts as an identifier of high-energy Q2 and Q4 velocity fluctuations in the upper shear layer, scatter plots of velocity fluctuations on the radial-axial shear plane (i.e., V_r' versus V_x') at the three locations marked by white dots in Fig. 12(c) across all three conditions are shown in Fig. 13. All velocity fluctuations in Fig. 13 were normalized by the rms value of V_x' at the mean reattachment location, which is denoted as σ. Additionally, the percentage values in each quadrant of this figure represent the percentage of velocity fluctuation events from the plotted ensemble that occur in that quadrant.

In Fig. 13, each row of scatter plots represents a fixed location across all conditions, and each column represents a fixed condition across all locations, using the same conditional sorting of snapshots for mode 2 as the previous figures. At all three locations, for the unconditional ensemble of velocity fluctuations, the high-energy fluctuations are split quite evenly between quadrants 2 and 4. Note that a correlation of velocity fluctuations aligning with either of these quadrants intrinsically defines a negative value of the kinematic Reynolds shear stress, which was identified throughout this flow in Fig. 12(b). When the snapshots are conditionally sorted for $a_2 < -1$ [Figs. 13(b), 13(e), and 13(h)], the balance of fluctuations in these scatter plots clearly shifts toward quadrant 2. For $a_2 < -1$, the percentage of fluctuations from each ensemble occurring in quadrant 2 increases by 9.5%, 17.5%, and 18.4% for the three locations, respectively. This percentage increase comes with a corresponding decrease in the number of Q4 events at each location. Looking at the other condition, $a_2 > +1$, the inverse of this is true [Figs. 13(c), 13(f), and 13(i)], where there is now a clear increase in fractional Q4 activity at each of the three locations with a corresponding decrease in Q2 activity.

Thus, the results of this section demonstrate that conditionally sorting the velocity field snapshots based on the sign of their corresponding POD coefficient for mode 2 acts as an identifier of high-energy Q2 and Q4 activity in the upper shear layer for negative and positive coefficients, respectively. Although not shown here for succinctness, the same is true for mode 3 and the lower shear layer, as positive coefficients for mode 3 identify high-energy Q2 events, and negative coefficients identify Q4 events. Given that these high-energy velocity fluctuations were demonstrated in previous work to be caused by upright and inverted hairpin vortex structures within this flow, it follows that modes 2 and 3 of this analysis act as identifiers of snapshots that measure planar slices of these high-energy coherent structures.

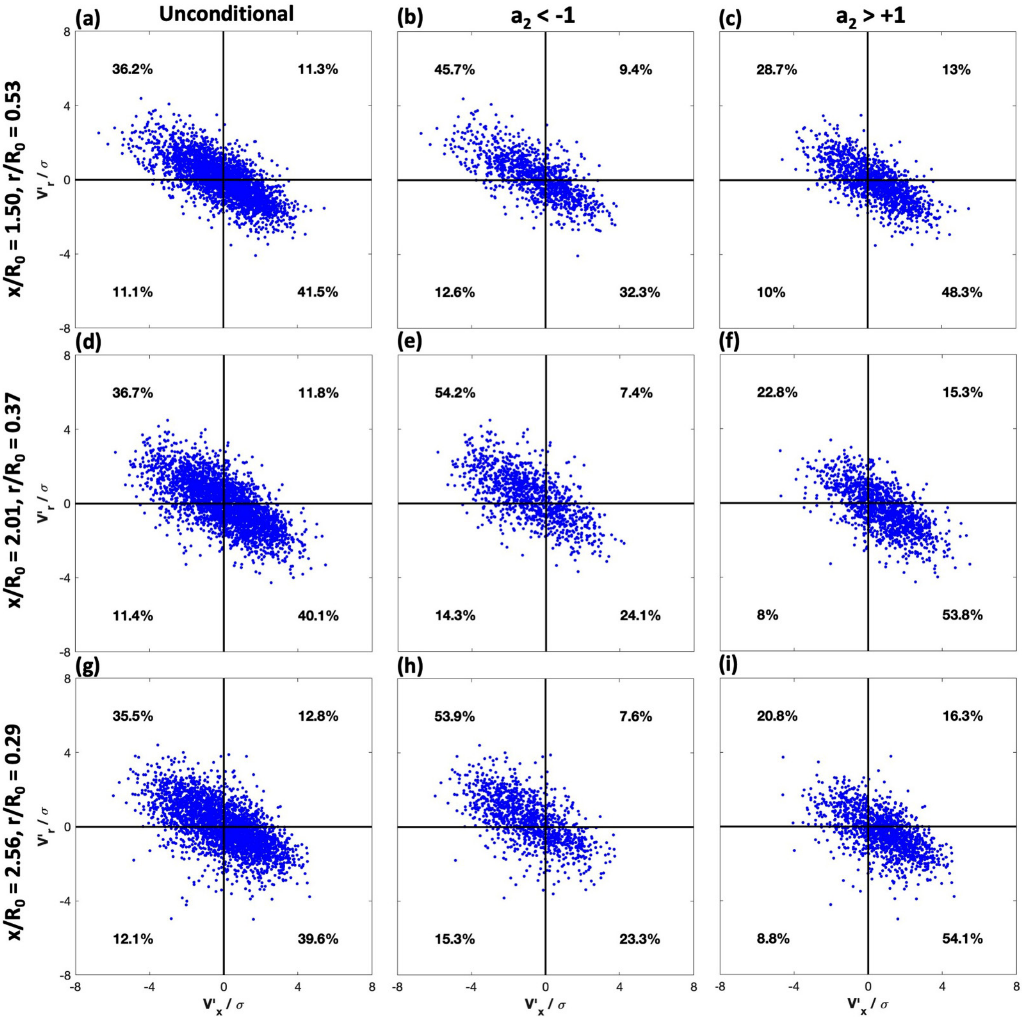

FIG. 13. Velocity fluctuation scatter plots at three separate high TKE locations in the shear layer for three different conditions each. Locations are identified by white dots in Fig. 12(c). Each row is a constant location and each column is a constant condition. [(a)–(c)] Location 1 (furthest upstream), [(d)–(f)] location 2 (middle location), and [(g)–(i)] location 3 (furthest downstream). Percentages represent the fraction of fluctuation realizations that exists in each respective quadrant for the conditional ensemble.

C. Influence on shear layer reattachment

The previous section demonstrated that POD modes 2 and 3 act as useful identifiers of coherent upright and inverted hairpins within this flow. The current section aims to identify the influence that these structures have on critical flow properties, such as reattachment length. By first conditionally sorting the snapshots of the flow for a higher statistical prevalence of either type of structure, then comparing the features of the conditionally averaged flow field to the unconditional flow, the differences in those features can be confidently interpreted as correlating to the presence of either type of structure. In particular, the influence of these structures on the entrainment characteristics of the shear layer is of interest, as it is ultimately these turbulent entrainment/detrainment interactions between the shear layer and recirculation region that determine the reattachment length and subsequent pressure loading on the cylinder base.

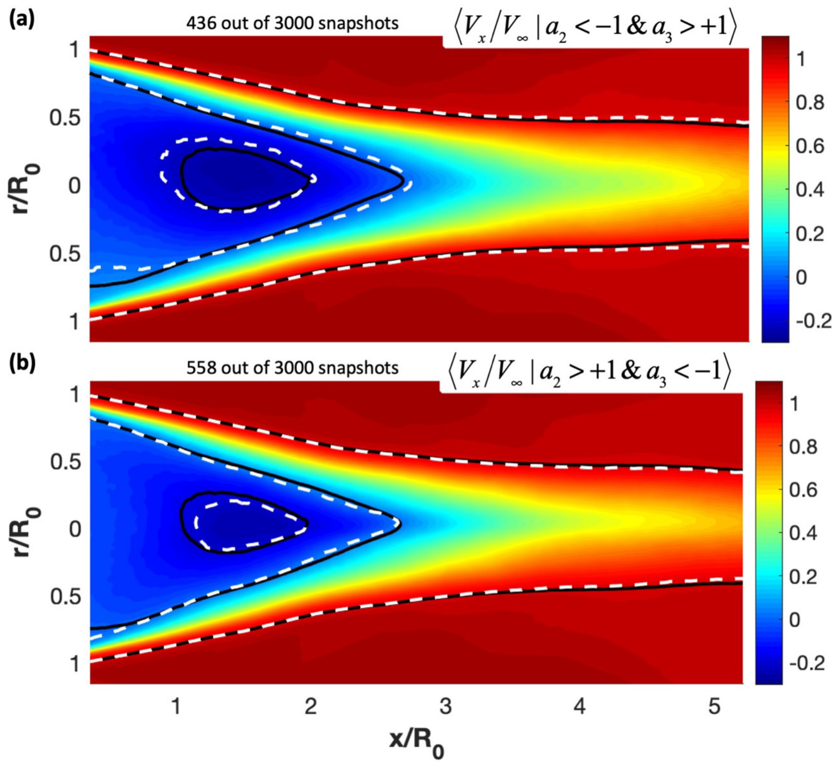

FIG. 14. (a) Conditional mean V_x/V_∞ given that $a_2 < -1$ and $a_3 > +1$ and (b) conditional mean V_x/V_∞ given that $a_2 > +1$ and $a_3 < -1$. Solid contours denote shear layer boundaries and the bulk region of relatively high-speed recirculating fluid. Black contours depict these features for the unconditional flow, and dashed white contours are for the conditional average.

There is currently no clear evidence that there exists a synchronicity of these Q2 and Q4 turbulent motions between both shear layers (i.e., in the absence of a very large-scale global flow motion, the dynamics of the two shear layers would be largely independent of one another). Although it is possible, and perhaps likely, that there is a global flow motion wherein the dynamics of one shear layer propagates and influences the other (such as a flapping or pulsing mechanism [3]), no such conclusions are assumed or drawn here. However, given that the total ensemble of snapshots is quite large ($N = 3000$), then even under the assumption that the shear layers develop independently of one another, there does exist a significant subset of snapshots for which both shear layers exhibit high-energy Q2 or Q4 motions simultaneous to one another. This condition would require snapshots that had a negative a_2 and a positive a_3 for high-energy Q2 events occurring in both shear layers, and vice versa for Q4 events. Figure 14 demonstrates the conditional velocity field averages using the conditions for modes 2 and 3 that correspond to Q2 events in both shear layers in Fig. 14(a), and the conditions for both modes corresponding to Q4 events in both shear layers in Fig. 14(b). For the two conditional averages, the size of the subset of snapshots that satisfied both conditions was 436 for the conditions corresponding to Q2 events, and 558 for the conditions corresponding to Q4 events. Note that the contour lines in this figure are the same as previous figures, wherein solid black contours depict the unconditional flow features, and dashed white contours are the conditionally averaged flow features.

From Fig. 14(a), as well as previously presented results, it is clear that when the flow is conditionally averaged for a higher prevalence of Q2 fluctuations, the shear layer growth rate along

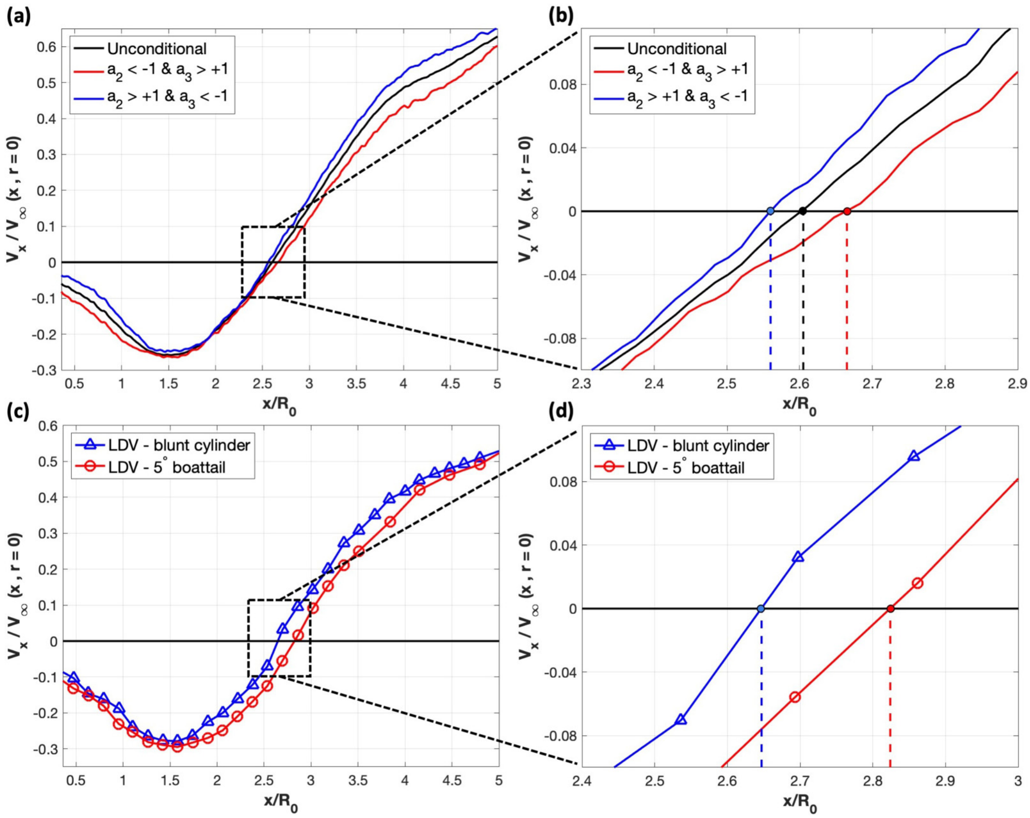

FIG. 15. (a) V_x/V_∞ at $r = 0$ for the current data, (b) enlarged view of panel (a), (c) V_x/V_∞ at $r = 0$ for the LDV data of Herrin and Dutton for both the blunt cylinder case and a 5° boat-tail case [12,16], and (d) enlarged view of panel (c). In panels (b) and (d), the dashed lines correspond to the reattachment location in each case.

the boundary separating it from the recirculation region is reduced compared to the unconditional case, and correspondingly, the reattachment location shifts downstream. The inverse is also true for conditional sorting based on Q4 events, in that the shear layer growth rate along this same boundary is now greater than the unconditional flow, with a corresponding shift upstream of the reattachment location. This conditional sorting based on like events in both shear layers across both modes allowed the mean reattachment point to remain on the central axis in these conditional averages, which makes it easier to clearly identify how the reattachment point shifts with an increased prevalence of either structure. This shift in the reattachment region is a direct result of modified entrainment/detrainment turbulent interactions along this boundary, which undoubtedly has a strong impact on the cylinder base pressure distribution.

Additionally, this conditionally resolved change in shear layer turbulence has a profound impact on the near-wake recovery, as the wake is thinner and recovers much more rapidly in the event of increased shear layer Q4 activity [Fig. 14(b)], with the wake being wider, and recovering more slowly in the event of increased shear layer Q2 activity [Fig. 14(a)]. Furthermore, these changes in the shear layer entrainment/detrainment rates also influence the recirculating flow, as the longer reattachment length exhibits higher reverse flow velocities and a larger bulk-recirculating fluid region, and vice versa for the shorter reattachment length. To more clearly demonstrate the influence that these conditional averages have on the location of shear layer reattachment, as well as to draw appropriate comparisons to other works in the literature, Fig. 15 shows the axial velocity as a line plot along the centerline (i.e., $r = 0$) for the unconditional case, as well as for both conditional cases shown in Fig. 14.

Figure 15(a) shows the full streamwise extent of velocity along the centerline for all three cases, and Fig. 15(b) shows an enlarged view of Fig. 15(a), centered on the reattachment point. The dashed lines in Fig. 15(b) denote the reattachment location for each of the three cases, which is identified as the location where the mean axial velocity vanishes along the centerline. The results previously identified in Fig. 14 are clearly reinforced here by Fig. 15, in that the conditional average corresponding to increased Q2 activity in the two shear layers shifts the reattachment point further downstream [red line in Fig. 15(b)], and vice versa for the Q4 conditions [blue line in Fig. 15(b)]. Also note that the effects of the conditional averages are even more pronounced in the far upstream and downstream portions of the centerline [Fig. 15(a)] than they are at reattachment, further demonstrating that a small shift in the reattachment length can accompany large changes in the global flow properties.

The reattachment comparison is supplemented by also drawing a comparison to the previous work of Herrin and Dutton [12,16], wherein LDV measurements of velocity were acquired in the same blunt cylinder case as the current work, in addition to the case of a 5° boat-tailed cylinder at the same free-stream Mach number. These boat-tail experiments demonstrated that a small shift downstream of the reattachment location directly correlates with a significant increase in the cylinder base pressure. Specifically, they found that a 6% shift downstream of the reattachment location (i.e., a shift from $x/R_0 = 2.65$ to $x/R_0 = 2.81$) for the blunt cylinder and boat-tail experiments, respectively, resulted in a 21% reduction in cylinder pressure drag. This demonstrates that even a slight modulation of the shear layer entrainment characteristics can have a profound impact on the resulting pressure loading.

Several clear comparisons can be drawn between Figs. 15(a) and 15(c). In the boat-tail cylinder case [red line in Fig. 15(c)], the shift downstream in the reattachment location also accompanies a slight increase in maximum reverse velocity in the recirculation region, as well as a reduced rate of recovery for the near-wake downstream of reattachment, compared to the blunt cylinder case. These same features can be observed in the conditionally averaged case corresponding to increased Q2 turbulence in the shear layers [the red line in Fig. 15(a)]. For this specific set of POD coefficient conditions, the three reattachment locations resolved in Fig. 15(b) are $x/R_0 = 2.56$, $x/R_0 = 2.61$, and $x/R_0 = 2.67$ for the Q4, unconditional, and Q2 cases, respectively (i.e., a 2.3% shift between the unconditional and Q2 cases, and a 1.9% shift between the unconditional and Q4 cases).

To provide additional validation that the features of the conditionally averaged flow field for increased Q2 activity matches that of the boat-tail cylinder case, line plots of TKE along the centerline for all three cases are shown in Fig. 16. Herrin and Dutton [16] demonstrated that in addition to the shift downstream in the reattachment location for the boat-tail case, there was also a reduction in TKE along the centerline. However, their experiments only measured two components of velocity and computed the TKE by assuming $R_{\theta\theta} = R_{rr}$ [Eq. (13)], which Ref. [4] demonstrated was not true in this flow, as $R_{\theta\theta}$ was found to be much larger than R_{rr} along the centerline. Nevertheless, the relative reduction in TKE magnitude along the centerline was found to also exist in the conditional case here corresponding to increased Q2 activity, demonstrated by the red line in Fig. 16. This reduction in turbulent energy along the centerline also correlates with the reduced wake recovery rate in this conditional case. For the other conditional case, the inverse is true, where the conditional average corresponding to increased Q4 activity demonstrates a slight increase in TKE along the centerline over the unconditional case (blue line in Fig. 16). These line plots for the conditional cases in Fig. 16 are quite noisy, due to the relatively small ensemble sizes used to calculate them, but the trends they indicate are clear and are consistent with the LDV results of Herrin and Dutton [16], including their relative relationship with the shear layer reattachment length.

Additionally, it should be pointed out that the magnitude of the condition placed on the POD coefficients in this analysis was arbitrary. Snapshots with a corresponding POD coefficient near zero for a given mode indicate that the dynamics of that mode were not significant during that

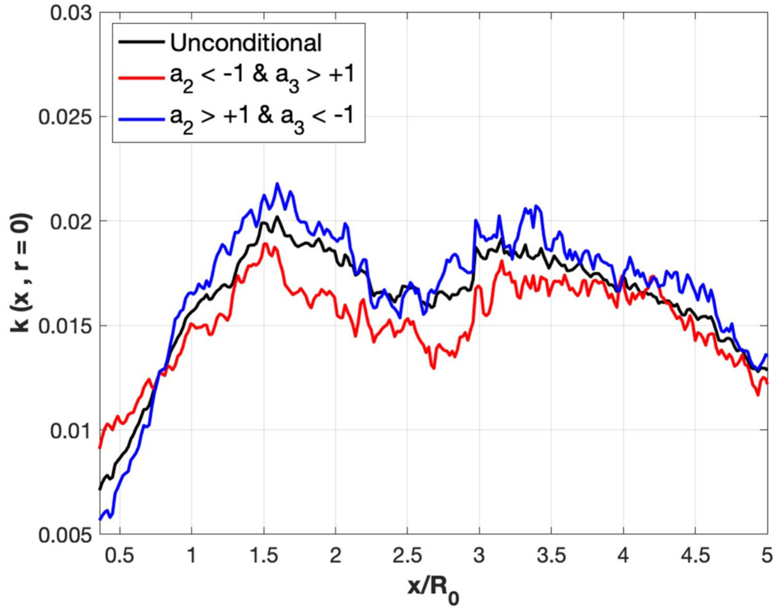

FIG. 16. TKE along $r = 0$ for each of the three cases.

specific snapshot. Correspondingly, the conditions on a_2 and a_3 needed to be set sufficiently far from zero, but the further away from zero they were set, the more reduced the conditional ensemble size became. This reduction in conditional ensemble size would then reduce the convergence of the conditional statistics. For example, if these conditions were set further away from zero, say to $a_2 < -2$ and $a_3 > +2$, then the results of Figs. 15(a) and 15(b) become more pronounced, and the conditional reattachment location depicted by the red line in Fig. 15(b) shifts even further downstream. Specifically, the conditions of $a_2 < -2$ and $a_3 > +2$ shifts the reattachment point to $x/R_0 = 2.7$, as opposed to $x/R_0 = 2.67$ for the conditions of $a_2 < -1$ and $a_3 > +1$ shown in Fig. 15, which is an additional 1.2% shift further downstream. The inverse is also true for the opposite condition, wherein if $a_2 > +2$ and $a_3 < -2$ are used, then the Q4 turbulence is more pronounced, and the reattachment location shifts even further upstream to a location of $x/R_0 = 2.54$, compared to $x/R_0 = 2.56$ for the conditions of $a_2 > +1$ and $a_3 < -1$.

Therefore, Fig. 15 is not necessarily intended to demonstrate quantitative values of the distance that the reattachment location shifts in each case, but instead to demonstrate the qualitative influence that each set of conditions (and thus, the identification of specific flow structures) has on the underlying flow. Comparisons with the boat-tail LDV data, which demonstrated a significant modulation in cylinder pressure drag for a relatively small shift in reattachment location, provide further confidence that the alterations to the mean flow for each set of conditions does indeed correlate with a corresponding change in cylinder pressure loading. Thus, from the evidence provided here, it appears that a higher than average prevalence of high-energy Q2 turbulence in the shear layers, which is indicative of upright hairpin structures, directly correlates with reduced shear layer growth rates, a downstream shift in the reattachment location, and subsequently, reduced cylinder pressure drag. Conversely, a higher than average prevalence of high-energy Q4 turbulence, which is indicative of inverted hairpin structures, directly correlates with increased shear layer growth rates, an upstream shift in the reattachment location, and increased cylinder pressure drag.

This result is quite significant, as it directly correlates the presence of these high-energy turbulent structures to the underlying entrainment characteristics of the separated shear layer. It should be pointed out, however, that this result does not necessarily demonstrate a direct causal relationship between these structures and modified shear layer entrainment rates (i.e., it is not necessarily true that the inverted/upright hairpins directly induce the turbulent entrainment/detrainment events). This analysis simply demonstrates that the increased prevalence of these structures directly correlates with the identified modulations of the underlying flow. Although it is possible that these structures directly induce these modulations to the shear layer growth rates through the magnified shearing mechanism along their inner arches, it is also possible that they cause these modulations to the mean entrainment/detrainment rates by inducing secondary instabilities in the flow, which then subsequently modify the growth rates. Future work will aim to investigate the direct mechanisms of shear layer entrainment/detrainment in this flow.

However, logically, it does seem reasonable to consider that the upright hairpins would directly induce the increased reattachment length, and vice versa for the inverted hairpins. In the downstream portions of the shear layer, the mean flow detrains fluid into the recirculation region to satisfy continuity requirements. The Q2 events induced by the upright hairpins directly oppose the mean detrained fluid, and thus, an increased prevalence of these structures in this region would act to reduce the mean detrainment flow rate. Alternately, the Q4 events induced by the inverted hairpins follow approximately the same direction as the mean detrained fluid, and an increased prevalence of these structures in this region would act to increase the mean detrainment flow rate. Recall from previous discussion that in this highly complex flow, the growth of the shear layer is not purely a function of fluid mass entrainment into the shear layer, as it nominally is in planar unseparated shear layers. If the shear layer growth were purely a function of mass entrainment into the shear layer, then the mean shear layer would actually decrease in thickness as it approached reattachment, which Fig. 4 demonstrated was not the case. Therefore, if the interpretation of the shear layer growth in this flow can be viewed more simply as directly correlating with the magnitude of the local entrainment/detrainment rates along the low-speed boundary, as both the literature and current analysis suggest is true, then the above analysis does indicate, even if it does not strictly prove, that the upright hairpins directly act to increase reattachment length and decrease pressure loading, and vice versa for the inverted hairpins.

V. CONCLUSIONS

The influence of coherent turbulent structures on the entrainment characteristics of a separated shear layer in a Mach-2.49 longitudinal cylinder wake was investigated using stereoscopic particle image velocimetry (SPIV) measurements. The method of snapshots proper orthogonal decomposition (POD) technique was used to decompose 3000 planar velocity field measurements into a set of spatially dependent turbulent modes. It was demonstrated that the POD coefficients for mode 2 acted as identifiers of snapshots that exhibited a high prevalence of Q2 and Q4 turbulent events in the upper shear layer, with the same being true of the lower shear layer and mode 3. Conditional averages of velocity based on POD coefficient sorting demonstrated that a higher prevalence of high-energy Q2 events in both shear layers (and subsequently, a lower prevalence of Q4's) directly correlates with reduced shear layer growth rates and an increased reattachment length. Conversely, conditional averages that corresponded to a higher prevalence of high-energy Q4 events (and subsequently, a lower prevalence of Q2's) in both shear layers correlates with increased shear layer growth rates and a reduced reattachment length.

Previous work by the authors, using tomographic PIV, demonstrated that high-energy Q2 events in the shear layer were caused by coherent upright hairpin vortices and that high-energy Q4 events were caused by inverted hairpin vortices, which are topologically inverted from the upright hairpins but demonstrate the same physical amplified shearing mechanism. Additionally, comparisons of these conditional SPIV results to previous laser Doppler velocimetry (LDV) measurements of this same flow field, as well as to LDV measurements acquired in the near wake of the same approach flow over a 5° boat-tailed cylinder configuration demonstrated clear consistencies in critical flow features. Although simultaneous pressure data were not acquired in the current experiments, similarities between the conditionally averaged SPIV flow field data and the LDV boat-tail data, as well as commonly agreed upon characteristics of separated shear layers in the literature, provide strong evidence that these conditionally averaged shifts in the reattachment length correspond to modulations in the cylinder pressure drag.

Therefore, these previously presented works, combined with the current analysis, demonstrate a clear correlation between the presence of upright hairpins and reduced shear layer growth rates, an increase in the reattachment length, and a postulated reduction in pressure drag, and vice versa for the inverted hairpins. Although the direct mechanisms of instantaneous fluid entrainment/detrainment between the shear layer and recirculation region in this flow are still unknown, a change in the statistical prevalence of these structures does clearly correlate with significant changes in the mean entrainment/detrainment rates. Therefore, the development of a flow control methodology that targets the formation mechanisms of these structures and successfully alters their formation, growth, or spatial distribution within the shear layer of this flow would undoubtedly have a significant influence on the resulting cylinder pressure loading.

ACKNOWLEDGMENTS

The authors would like to thank the U.S. Army Research Office for their support of this work with DURIP Equipment Grant No. W911NF-14-1-0404 and Research Grant No. W911NF-15-1-0194. The first author would also like to recognize the financial support provided by the NDSEG fellowship program with sponsorship from the Air Force Office of Scientific Research.

---

[1] V. A. Amatucci, J. C. Dutton, D. W. Kuntz, and A. L. Addy, Two-stream, supersonic, wake flowfield behind a thick base, part I: General features, AIAA J. **30**, 2039 (1992).

[2] F. Scarano and B. W. van Oudheusden, Planar velocity measurements of a two-dimensional compressible wake, Exp. Fluids **34**, 430 (2003).

[3] R. Humble, F. Scarano, and B. W. van Oudheusden, Unsteady flow organization of compressible planar base flows, Phys. Fluids **19**, 076101 (2007).

[4] B. M. Kirchner, J. V. Favale, G. S. Elliott, and J. C. Dutton, Three-component turbulence measurements and analysis of a supersonic, axisymmetric base flow, AIAA J. **57**, 2496 (2019).

[5] C. Bourdon and J. C. Dutton, Planar visualizations of large-scale turbulent structures in axisymmetric supersonic separated flows, Phys. Fluids **11**, 201 (1999).

[6] R. D. Sandberg, Numerical investigation of turbulent supersonic axisymmetric wakes, J. Fluid Mech. **702**, 488 (2012).

[7] G. L. Brown and A. Roshko, On density effects and large structure in turbulent mixing layers, J. Fluid Mech. **64**, 774 (1974).

[8] R. D. Sandberg and H. F. Fasel, Numerical investigation of transitional supersonic axisymmetric wakes, J. Fluid Mech. **563**, 1 (2006).

[9] F. Simon, S. Deck, P. Guillen, P. Sagaut, and A. Merlen, Numerical simulation of the compressible mixing layer past an axisymmetric trailing edge, J. Fluid Mech. **591**, 215 (2007).

[10] N. T. Clemens and M. G. Mungal, Large-scale structure and entrainment in the supersonic mixing layer, J. Fluid Mech. **284**, 171 (1995).

[11] L. Rollstin, Measurement of inflight base-pressure on an artillery-fired projectile, in *Atmospheric Flight Mechanics Conference* (AIAA, Monterey, CA, 1987), pp. 195–201.

[12] J. L. Herrin and J. C. Dutton, Supersonic base flow experiments in the near wake of a cylindrical afterbody, AIAA J. **32**, 77 (1994).

[13] S. B. Pope, The evolution of surfaces in turbulence, Int. J. Eng. Sci. **26**, 445 (1988).

[14] J. Westerweel, C. Fukushima, J. M. Pedersen, and J. C. R. Hunt, Mechanics of the Turbulent-Nonturbulent Interface of a Jet, Phys. Rev. Lett. **95**, 174501 (2005).

[15] J. Westerweel, C. Fukushima, J. M. Pedersen, and J. C. R. Hunt, Momentum and scalar transport at the turbulent/non-turbulent interface of a jet, J. Fluid Mech. **631**, 199 (2009).

[16] J. L. Herrin and J. C. Dutton, Supersonic near-wake afterbody boattailing effects on axisymmetric bodies, J. Spacecr. Rockets **31**, 1021 (1994).
[17] J. L. Herrin and J. C. Dutton, Effect of a rapid expansion on the development of compressible free shear layers, Phys. Fluids **7**, 159 (1995).
[18] J. L. Herrin and J. C. Dutton, The turbulence structure of a reattaching axisymmetric compressible free shear layer, Phys. Fluids **9**, 3502 (1997).
[19] L. Sirovich, Turbulence and the dynamics of coherent structures part 1: Coherent structures, Q. Appl. Math. **45**, 561 (1987).
[20] P. E. Dimotakis, Two-dimensional shear layer entrainment, AIAA J. **24**, 1791 (1986).
[21] R. Jahanbakhshi and C. K. Madnia, Entrainment in a compressible turbulent shear layer, J. Fluid Mech. **797**, 564 (2016).
[22] S. Piponniau, E. Collin, P. Dupont, and J. F. Debiéve, Reconstruction of velocity fields from wall pressure measurements in a shock wave/turbulent boundary layer interaction, Int. J. Heat Fluid Flow **35**, 176 (2012).
[23] D. Estruch-Samper and G. Chandola, Separated shear layer effect on shock-wave/turbulent-boundary-layer interaction unsteadiness, J. Fluid Mech. **848**, 154 (2018).
[24] S. Kawai and K. Fujii, Computational study of a supersonic base flow using hybrid turbulence methodology, AIAA J. **43**, 1265 (2005).
[25] M. Samimy and S. K. Lele, Motion of particles with inertia in a compressible free shear layer, Phys. Fluids **3**, 1915 (1991).
[26] J. R. Janssen and J. C. Dutton, Time-series analysis of supersonic base-pressure fluctuations, AIAA J. **42**, 605 (2004).
[27] G. Berkooz, P. Holmes, and J. L. Lumley, The proper orthogonal decomposition in the analysis of turbulent flows, Annu. Rev. Fluid Mech. **25**, 539 (1993).
[28] P. L. van Gent, B. W. van Oudheusden, and F. F. J. Schrijer, Determination of mean pressure from PIV in compressible flows using the Reynolds-averaging approach, Exp. Fluids **59**, 1 (2018).
[29] K. E. Meyer, J. M. Pedersen, and O. Ozcan, A turbulent jet in crossflow analysed with proper orthogonal decomposition, J. Fluid Mech. **583**, 199 (2007).
[30] F. Stella, N. Mazellier, P. Joseph, and A. Kourta, Scaling of separated shear layers: An investigation of mass entrainment, J. Fluid Mech. **826**, 851 (2017).
[31] K. U. Kim, G. S. Elliott, and J. C. Dutton, Three-dimensional experimental study of compressibility effects on turbulent free shear layers, AIAA J. **58**, 133 (2020).
[32] P. Bradshaw, The effect of mean compression or dilatation on the turbulence structure of supersonic boundary layers, J. Fluid Mech. **63**, 449 (1974).
[33] A. J. Smits, J. A. Eaton, and P. Bradshaw, The effect of short regions of high surface curvature on turbulent boundary layers, J. Fluid Mech. **94**, 209 (1979).
[34] A. J. Smits and D. H. Wood, The response of turbulent boundary layers to sudden perturbations, Annu. Rev. Fluid Mech. **17**, 321 (1985).
[35] B. M. Kirchner, G. S. Elliott, and J. C. Dutton, Hairpin vortex structures in a supersonic, separated, longitudinal cylinder wake, Phys. Fluids **32**, 046103 (2020).
[36] D. Papamoschou and A. Roshko, The compressible turbulent shear layer: An experimental study, J. Fluid Mech. **197**, 453 (1988).
[37] B. Knight and L. Sirovich, Kolmogorov Inertial Range for Inhomogeneous Turbulent Flows, Phys. Rev. Lett. **65**, 1356 (1990).
[38] P. Das and A. De, Numerical investigation of flow structures around a cylindrical afterbody under supersonic conditions, Aerospace Sci. Technol. **47**, 195 (2015).
[39] J. M. Wallace, H. Eckelmann, and R. S. Brodkey, The wall region in turbulent shear flow, J. Fluid Mech. **54**, 39 (1972).
[40] M. Sieber, C. O. Paschereit, and K. Oberleithner, Spectral proper orthogonal decomposition, J. Fluid Mech. **792**, 798 (2016).
[41] A. Towne, O. T. Schmidt, and T. Colonius, Spectral proper orthogonal decomposition and its relationship to dynamic mode decomposition and resolvent analysis, J. Fluid Mech. **847**, 821 (2018).

[42] K. Taira, S. L. Brunton, S. T. M. Dawson, C. W. Rowley, T. Colonius, B. J. McKeon, O. T. Schmidt, S. Gordeyev, V. Theofilis, and L. S. Ukeiley, Modal analysis of fluid flows: An overview, AIAA J. **55**, 4013 (2017).

[43] M. A. Mendez, M. Balabane, and J. M. Buchlin, Multi-scale proper orthogonal decomposition of complex fluid flows, J. Fluid Mech. **870**, 988 (2019).

[44] C. W. Rowley and T. M. Dawson, Model reduction for flow analysis and control, Annu. Rev. Fluid Mech. **49**, 387 (2017).

[45] R. J. Adrian, B. G. Jones, M. K. Chung, Y. Hassan, C. K. Nithianandan, and A. T. C. Tung, Approximation of turbulent conditional averages by stochastic estimation, Phys. Fluids A **1**, 992 (1989).

[46] R. J. Adrian, Hairpin vortex organization in wall turbulence, Phys. Fluids **19**, 041301 (2007).

[47] G. E. Elsinga, R. J. Adrian, B. W. Van Oudheusden, and F. Scarano, Three-dimensional vortex organization in a high-Reynolds-number supersonic turbulent boundary layer, J. Fluid Mech. **644**, 35 (2010).

[48] S. Ghaemi and F. Scarano, Counter-hairpin vortices in the turbulent wake of a sharp trailing edge, J. Fluid Mech. **689**, 317 (2011).

[49] J. Zhou, R. J. Adrian, S. Balachandar, and T. M. Kendall, Mechanisms for generating coherent packets of hairpin vortices in channel flow, J. Fluid Mech. **387**, 353 (1999).